M. R. Rahul,[1] Sumanta Samal,[2] and Gandham Phanikumar[1]

Hot Deformation Behavior and Microstructural Characterization of CoCrFeNiNb$_{0.45}$ Eutectic High Entropy Alloy

Reference

ABSTRACT

In recent years, several multicomponent alloys of near equiatomic composition (also known as high-entropy alloys) with excellent mechanical properties have been developed. In this study, a eutectic high entropy alloy, CoCrFeNiNb$_{0.45}$, was chosen for a hot deformation study. The alloy consists of a primary face-centered cubic (FCC) phase (CoCrFeNi rich) and a eutectic region between the FCC and Laves phase (Co$_2$Nb type). The combination of FCC and eutectic region is expected to provide better strength and ductility. Hot compression tests were carried out at different strain rates of 0.001, 0.1, 1, and 10 s^{-1} with varying temperatures of 1,073, 1,173, 1,273, and 1,323 K. The optimum processing window was identified by plotting processing maps, and the instability region was verified using multiple parameters. Constitutive equation relating stress, strain rate, and temperature is established. The optimum processing condition was correlated with the microstructural characterization, and instability was characterized with cracks on the specimen. Finite element simulation was carried out, taking the flow curve as input and correlating the strain field distribution with the microhardness variation. These studies are intended to contribute to an integrated computational materials engineering approach to developing these alloys toward a product.

Keywords

eutectic high-entropy alloy, flow curves, processing maps, finite element analysis, integrated computational materials engineering approach

Introduction

The design and development of materials with simultaneous improvement in strength and ductility is a challenge. The material design domain has expanded from principal element–based approaches to multiprincipal element approaches with the advent of a new alloy design strategy by Yeh et al.[1,2] is popularly referred to as high-entropy alloys (HEAs). It has been shown recently that HEAs exhibit remarkable properties, such as high strength, better ductility, good corrosion, and oxidation resistance, etc.[3–6] The good combination of strength and ductility can be achieved by developing composite microstructures that consisting of hard and soft phases. Although the hard phase provides high strength, the soft phase will contribute to the ductility. Such a strategy has been used in the development of dual phase steels, $\alpha + \beta$ titanium alloys, etc.[7] It is reported in open literature that some HEAs show the formation of multiple phases[4,8–10] with unique phase equilibria. The eutectic HEAs (EHEAs) are a new class of multiphase HEAs[11] and are technologically considered as important engineering materials because of good castability, microstructure stability, and high mechanical properties. It is to be noted that the EHEAs show the microstructure consisting of face-centered cubic (FCC) + body-centered cubic (BCC) phases,[11,12] FCC + Laves phases,[13,14] and BCC + Sigma phases.[15] It is evident that EHEAs with FCC + Laves phases, such as $FeCoNiCrTa_x$,[16] $FeCoNiCrNb_x$,[14] and $FeCoNiCrZr_x$,[17] exhibit microstructural change with variation of tantalum, niobium, and zirconium concentration, respectively. The room temperature mechanical properties in EHEAs show a good combination of strength and ductility, which is attributed to a selection of composition and alloying elements in HEA systems[16] by a combination of experiments and thermodynamic estimates. It is reported that the $FeCoNiCrNb_x$ alloys that consist of FCC and eutectic mixture show promising properties with better strength and ductility combinations and also exhibit good thermal stability while annealing below 1,173 K.[18] The precipitation behavior of $FeCoNiCrNb_{0.25}$ alloy, annealed at 1,023K, also shows the formation of FCC basket weave–like structure.[19] It is reported that the strength is enhanced because of the formation of precipitates in the proeutectic phase. In this study, we explore the premise that EHEAs with proeutectic FCC phase with eutectic region in the interdendritic spaces could be a promising candidate for high-temperature application.

Optimization of thermomechanical processing route is necessary for industrial application of newly designed alloys. High-temperature processing of alloys using forging, rolling, extrusion, etc., are critical steps for futuristic design of the components for structural applications. The processing behavior of the alloy can be predicted based on the flow curves obtained during high-temperature compression tests.[20,21] The processing maps generated based on the flow stress data can be used to identify the stable and unstable processing conditions. In this study, an EHEA that has a hypoeutectic composition of $FeCoNiCrNb_{0.45}$ was chosen for high temperature deformation study. Integration of computer simulations and experimental studies is necessary in reducing the time scale for development of engineered products. The integrated computational materials engineering (ICME) provides the framework for development of novel product by integrating different scales ranging from electronic or atomic level to the product development at the macroscopic level. The synergistic effect of experimental and simulation methods can happen at different length scales as required by the critical issues in the development of the alloy. In the present investigation, the alloy design has been carried out by integrating the experimental technique with thermodynamic simulation methods using Thermo-Calc software prediction. Thus, a reduced number of experimental trials were needed. Secondly, integrating the finite element simulation method with different process conditions helps to test the component feasibility at different geometrical conditions and to determine microstructure gradients that arise out of thermal/strain rate gradients in an actual component being manufactured. In this study, we tried to generate a process flow from alloy design to hot deformation for component development with the help of Thermo-Calc prediction, designed experiments, and finite element simulations by establishing an optimum processing window. The processing map is developed based on the flow stress data from hot deformation tests at combinations of various temperatures and strain rates. Microstructural evolution during deformation at various processing conditions was correlated with the processing map developed at a true strain of 0.65 and the strain field distribution within the specimen was established based on the finite element method (FEM) simulation. Implementation the ICME approach was attempted, from alloy design to the development of the optimum process condition, for the current alloy.

Experimental Details

FeCoNiCrNb$_{0.45}$ EHEA was prepared using vacuum arc melting followed by the suction casting technique. An arc-melted button of around 20 g was prepared using elements of purity 99.9 % in a chamber backfilled with argon. The button was flipped and remelted five times to homogenize the alloy. The suction cast cylindrical rod—6 mm in diameter and 70 mm long—was cut to 9-mm-long rods in order to perform compression tests. A high-temperature compression test was carried out using Gleeble 3800 in a Hydrawedge module in the facility at Indian Institute of Technology Madras. The compression test was carried out at temperatures of 1,073, 1,173, 1,273, and 1,323 K, with strain rates of 0.001, 0.1, 1, and 10 s^{-1}. A graphite foil with nickel paste was used in between the specimen and anvil to get better conductivity as well as to reduce friction. The heating rate of 5 K/s with a soaking time period of 5 minutes was used. The compression test was carried out in strain rate control condition with a total true strain of 0.69, and microstructure after deformation was arrested by quenching the specimen with water. The compressed and as-cast specimens were polished using emery papers with different grades and were fine polished using alumina and colloidal silica for characterization. The suction cast and compressed specimens were characterized using scanning electron microscopy (SEM; Quanta400) in back scattered electron (BSE) mode to distinguish various phases in the microstructure using elemental contrast. The elemental mapping and compositional analysis were carried out using a Bruker energy dispersive spectroscopy (EDS) attached with Quanta 400 SEM. The microhardness measurements were performed on the selected specimens with load of 4.9033 N (500 gf) and dwell time of 10 seconds. The microhardness measurement was taken by considering the strain field distribution from finite element simulation and the specimens for hardness measurements are chosen from unstable (1,323 K at strain rate of 10 s^{-1}) and high-efficiency region (1,323 K at strain rate of 0.1 s^{-1}).

Results and Discussion

THERMODYNAMIC PREDICTION

Figure 1A shows the plot between the amount of phases versus temperature, which is obtained from the thermodynamic simulation using Thermo-Calc prediction using the TCHEA2 database. The thermodynamic prediction (**fig. 1A**) shows that the FeCoNiCrNb$_{0.45}$ alloy consists of FCC + Laves phase forming from the liquid, which matches the previous reports for this HEA system.[14] The phase fraction versus temperature plot shows around 70 % of FCC phase and the remaining Laves phase. The plot also confirms that formation of other equilibrium phases below 1,070 K can be expected to form at longer duration of heat treatment. The temperature selected for hot deformation was lying in the two-phase region (FCC + Laves) and was not expected to form any other phases within the short span of the experiment. The nonequilibrium microstructure formation during the solidification can be predicted by the Scheil calculation (**fig. 1B**). From the Scheil calculation, the solidification pathway can be established as Liquid → FCC + Liquid followed by eutectic reaction Liquid → FCC + Laves. The BSE-SEM image of the suction cast specimen (**fig. 1C**) reveals the presence of primary FCC dendritic structure (i.e., FeCoNiCr-rich phase) and interdendritic eutectic mixture (i.e., FCC + Laves phase mixture with interlamellar spacing of around 350 nm), which compares well with the earlier reports of hypoeutectic compositions of this system.[19] Primary dendritic phase was rich in iron, cobalt, nickel, and chromium, and the Laves phase is enriched with niobium. The x-ray powder diffraction (XRD) results shown in **figure 1D** confirm that the specimen consists of FCC and Laves phase, which matches the prediction by Thermo-Calc. The prediction from the Thermo-Calc was verified using SEM and XRD characterization, which, in turn, reduced the number of experiments associated with the design of alloy compared with the conventional alloy design method.

FLOW CURVES OF FeCoNiCrNb$_{0.45}$ UNDER COMPRESSION

Figure 2 shows the true stress versus true plastic strain variation at different temperatures and at strain rates of 0.001, 0.1, 1, and 10 s^{-1}. The flow stress decreased with the increase in temperature, and it increased with the

(*A*)

(*B*)

(*C*)

(*D*)
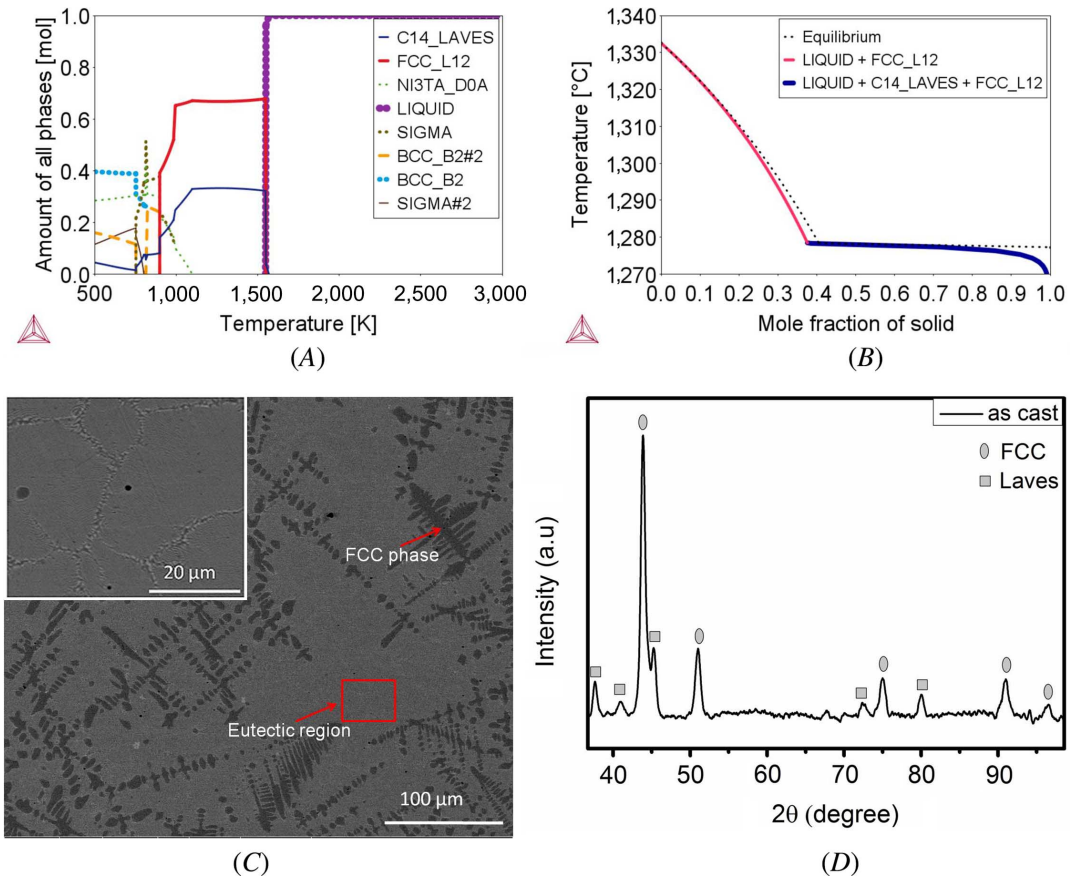
increase in the strain rate. The flow stress increased with the increase in strain and reached a peak, which was followed by a decrease with further increase in the strain. The increase in stress up to peak stress may be attributed to the strain hardening. The flow stress behavior is similar to other EHEAs reported in literature.[22] The material softening is observed to occur after the peak stress at all testing conditions. The flow softening is typically attributed to recrystallization, eutectic coarsening, eutectic breakage, or Laves phase breakage, etc. Eutectic coarsening through increase in interlamellar spacing could reduce the strength according to the Hall Petch relation ($\sigma_{ye} = \sigma_{0e} + k_H \lambda_e^{(-1/2)}$; where σ_{ye} is the yield strength of the material, σ_{0e} is the friction stress, k_H is the Hall Petch slope, and λ_e is the characteristic length). Eutectic coarsening will result in loss of lamellar morphology, allowing easy movement of dislocations and thus softening. In some cases, after softening in the material, the flow curve shows a steady-state nature, which may be attributed mainly to recrystallization.

CONSTITUTIVE MODELING OF FLOW CURVES

Developing an appropriate constitutive equation helps in correlating process parameters such as temperature, strain rate, and flow stress for a given extent of strain. In this study, a strain of 0.65 corresponds to the steady state condition and is used to generate the constitutive equation.

FIG. 2 True stress versus true plastic strain curves at strain rate conditions of (*A*) 0.001 s^{-1}, (*B*) 0.1 s^{-1}, (*C*) 1.0 s^{-1}, and (*D*) 10.0 s^{-1}.
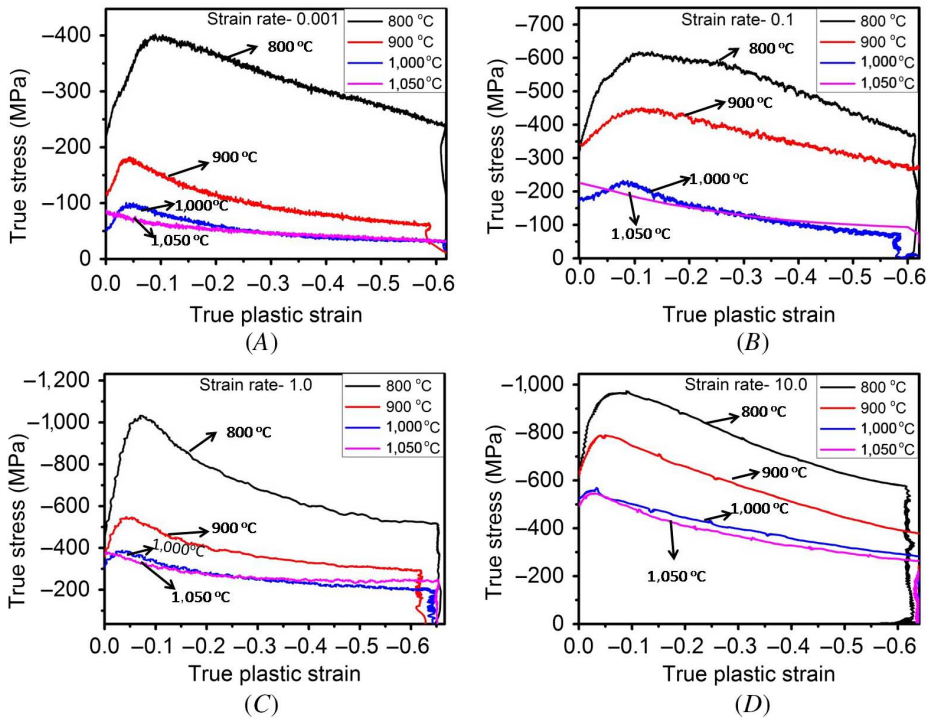
CALCULATION OF MATERIALS CONSTANTS

The flow stress, temperature, and strain rate dependence can be expressed by a sine hyperbolic Arrhenius-type equation proposed by Sellars and McTegart[23,24]

The equation can be written as:

$$\dot{\varepsilon} = A[\sin h(\alpha\sigma)]^n \exp\left[\frac{-Q}{RT}\right] \tag{1}$$

where the material constants A and α can be calculated from the test data obtained during hot compression experiments, $\dot{\varepsilon}$ is the strain rate, σ is the peak stress or steady state stress. The stress at 0.65 strain was taken for calculation in this study. Temperature (T) is expressed in Kelvin, and n is the stress exponent. R is the universal gas constant. The hot workability is governed by different deformation mechanisms that can be correlated with the activation energy (Q) calculated in corresponding conditions; in this study, the Q-value calculation was limited to steady state condition of true strain 0.65.

The function $[\sinh(\alpha\sigma)]^n$ in equation (1) can be expressed as follows:

$$[\sinh(\alpha\sigma)]^{n=\sigma^n} \quad \text{for } \alpha\sigma < 0.8 \quad \text{or} \quad = \exp(\beta\sigma) \quad \text{for } \alpha\sigma > 1.2 \tag{2}$$

where α, β, and n are constants, which are related to each other by the following equation:

$$\alpha = \beta/n \tag{3}$$

Figure 3A shows the plot between ln (strain rate) versus true stress at different temperatures from 1,073 to 1,323 K, and the slope of the linear fit gives the constant β. The average value of β calculated is 0.029. **Figure 3B** shows the plot between ln (strain rate) versus ln (true stress) at different testing temperature conditions, and the

FIG. 3 (*A*) Plot between ln (strain rate) and true stress, (*B*) ln (strain rate) versus ln (true stress), (*C*) ln (sinh($\alpha\sigma$)) versus (1/ *T*), and (*D*) ln (strain rate) versus ln (sinh($\alpha\sigma$)), where α is material constant, σ is true stress at strain condition of 0.65, and *T* is temperature in Kelvins.
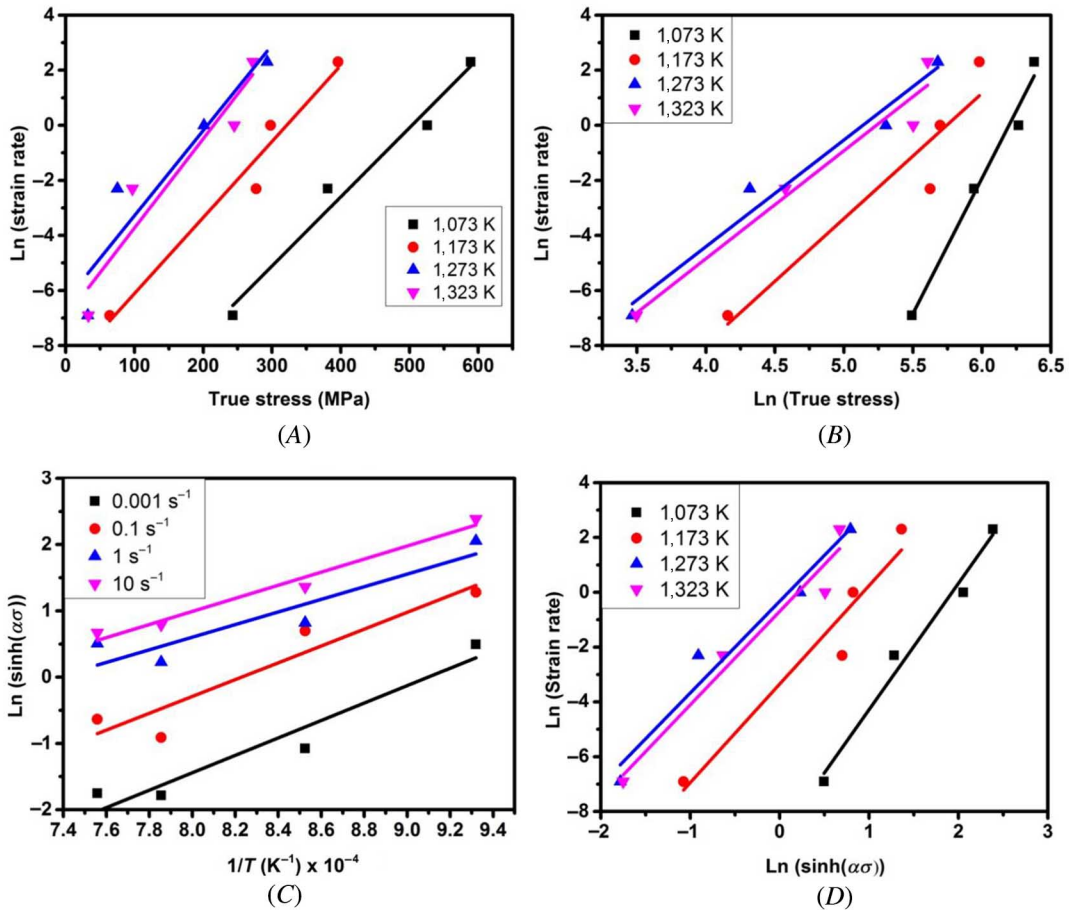
slope of the corresponding linear fit will give the value of *n* (stress exponent). The average value is determined to be 5.544. The value of α can be calculated as 0.00523 from these constants. The constitutive equation in this study was developed with the function [sinh ($\alpha\sigma$)]^n instead of using power law or exponential equation.

CALCULATION OF ACTIVATION ENERGY

The hot deformation behavior can be correlated with the activation energy (*Q*) required for the plastic deformation of studied EHEA. The activation energy can be calculated by the following modification in equation (1).

Taking the logarithm of both sides of equation (1), we get:

$$\ln \dot{\varepsilon} = \ln A + n \ln[\sinh(\alpha\sigma)] - \frac{Q}{RT} \tag{4}$$

After differentiating equation (4), we can write *Q* as follows:

$$Q = R\left\{\frac{\partial \ln \dot{\varepsilon}}{\partial \ln[\sinh(\alpha\sigma)]}\right\}_T \left\{\frac{\partial \ln[\sinh(\alpha\sigma)]}{\partial(1/T)}\right\}_{\dot{\varepsilon}} \tag{5}$$

The differential values of equation (5) can be calculated from the slope of **figure 3C** and **3D**, and its average value can be considered for Q-value calculation. The average activation energy of deformation was calculated to be 351.629 kJ/mol at a strain of 0.65. The calculated activation energy for the presently studied EHEA was comparable to previously reported EHEAs.[22]

CALCULATION OF ZENER-HOLLOMAN PARAMETER

The value of constant A in equation (1) can be identified by the use of the Zener-Hollomon parameter (Z). The Z-parameter correlates with the temperature, strain rate, and its effect on the flow stress of the material. The constitutive equation given in equation (1) can be modified to accommodate the Z-parameter, which is given as follows:

$$Z = \dot{\varepsilon} \exp\left(\frac{Q}{RT}\right) = A[\sinh(\alpha\sigma)]^n \tag{6}$$

Taking the logarithm of both sides of equation (8), we get:

$$\ln Z = \ln A + n \ln[\sinh(\alpha\sigma)] \tag{7}$$

Figure 4 shows the plot between ln Z versus ln (sinh ($\alpha\sigma$)), where the intercept on the y-axis is ln$A$ and the slope is n. The plot shows the linear increase in the ln Z value with ln (sinh ($\alpha\sigma$)), which confirms the applicability and accuracy of the constitutive model. Therefore, the constitutive equation that describes the flow stress of the multicomponent EHEA as a function of $\dot{\varepsilon}$ and T at strain (ε) of 0.65 can be written as follows:

$$\dot{\varepsilon} = 1.047 \times 10^{14}[\sinh 0.00523\sigma]^{3.59} \exp\left(\frac{351,629}{RT}\right) \tag{8}$$

## STRAIN RATE SENSITIVITY AND PROCESSING MAP

The strain rate sensitivity values (m) can be calculated by the following equation:

$$m = \left(\frac{\partial \ln \sigma}{\partial \ln \dot{\varepsilon}}\right)_{T,\varepsilon} \tag{9}$$

The m values are calculated at a strain condition of 0.65 in the presently studied EHEA. The m values can be used to identify the optimum processing window. In general, the regions with a negative m value can be considered as an unstable regime. In this study, m is positive throughout the domain. Therefore, the regions with lower values of m ($m < 0.1$) can be considered low-efficiency regions. At higher values of m, the window will be

FIG. 4

Plot shows the relation between Zener-Hollomon parameter (Z) and true stress (σ) at 0.65 strain
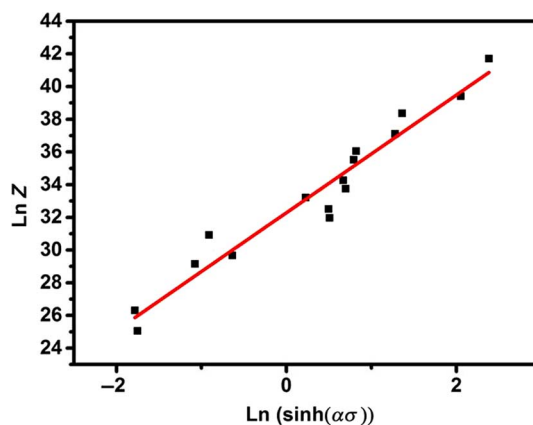
considered as the optimum for processing the material.[25] Based on the m value, the alloy shows the optimum processing window (fig. 5A) to be at a temperature above 1,200 K with a strain rate range of 0.01–1 s^{-1}, and a temperature range of 1,100–1,200 K with a strain rate range of 0.001–0.01 s^{-1}, which was verified by establishing the processing map.

Manufacturing processes, such as forging and rolling, involve bulk hot deformation processing of the material. It is necessary to understand the flow behavior and the identification of the optimum processing window for efficient and defect-free processing of the material. The processing map of the FeCoNiCrNb$_{0.45}$ is generated

FIG. 5 (A) Shows the strain rate sensitivity map, (B) processing map, (C) $\dot{m}$, (D) s, and (E) $\dot{s}$ at 0.65 strain condition, where the parameters $\dot{m}$, s, and $\dot{s}$ depend on the temperature, stress, and strain rate.
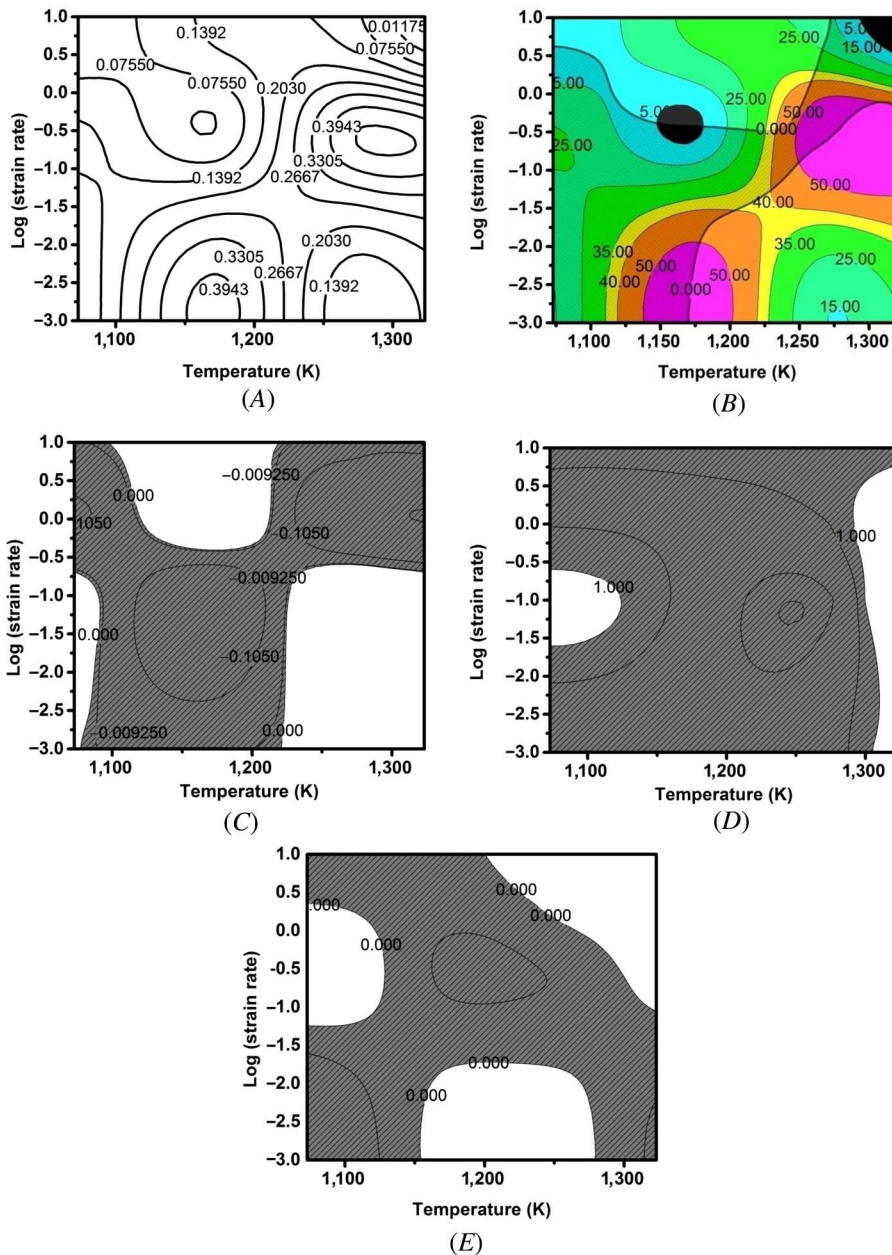
from the flow curve data in the present study and can be used as an efficient tool to identify proper working conditions. The processing map is constructed based on the dynamic material modeling (DMM),[20] where the material undergoes a dynamic and irreversible process. It is important to note that the superimposition of instability map on power dissipation map produces the processing map. **Figure 5B** shows the processing map for the studied EHEA at true strain of 0.65. The procedure for generating the efficiency map and instability map are explained elsewhere.[20,22] The hatched region on the processing map shows the instability region, whereas the color contours show the efficiency map with corresponding efficiency on the contour border. The processing map shows that the optimum processing domains for the presently studied EHEA are greater than 1,250 K with a strain rate between 0.1 and 1 s^{-1} and a temperature between 1,175 and 1,200 K with strain rate between 0.001 to 0.01 s^{-1}. This optimized window was narrower than the processing window obtained from the larger m value region. DMM also proposes other parameters, such us $\dot{m}$, s, and $\dot{s}$, which are expained in the literature.[26–29] The gray-hatched region on the map (**fig. 5C–E**) of these parameters indicates the safe domain in which the current alloy can be worked. The $\dot{m}$ and s contours show that the region 1,175–1,200 K with a strain rate between 0.001–0.01 s^{-1} can be considered as optimum for the alloy and also suggests that the $\dot{s}$ map can't be used to predict for the current alloy.

MICROSTRUCTURAL VARIATION AND CORRELATION WITH PROCESSING MAP

Figure 6 shows the BSE-SEM images of deformed specimens at selected stable and unstable conditions. **Figure 6A** and **6B** shows the microstructures at 1,323 K at strain rates of 0.001 s^{-1} (in stable condition)

FIG. 6   BSE-SEM images of specimen (*A*) 1,323 K with strain rate of 0.001 s^{-1}, (*B*) 1,323 K with strain rate of 0.1 s^{-1}, (*C*) 1,323 K with strain rate of 10 s^{-1} (inset shows the crack propagating in the Laves phase), and (*D*) 1,173 K with strain rate of 0.001 s^{-1}.
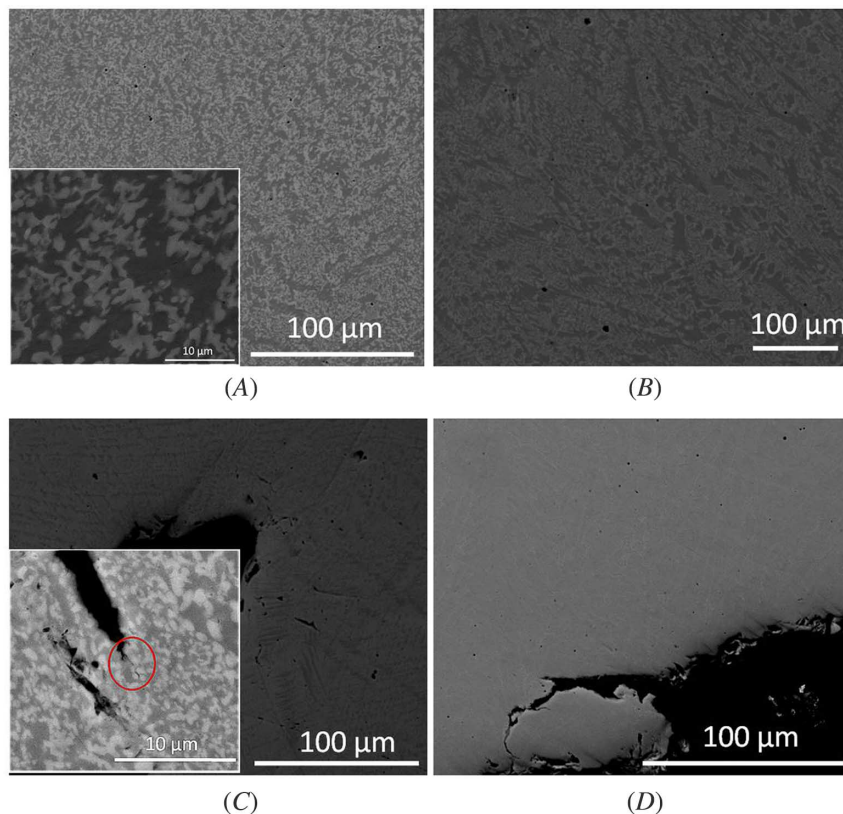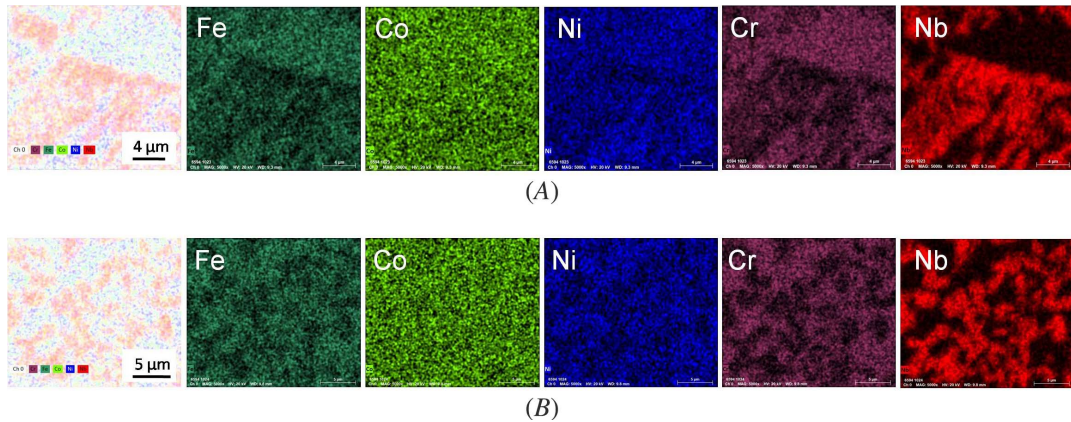

(*A*)

(*B*)

(*C*)

(*D*)

FIG. 7   SEM-EDS mapping of specimen (*A*) at 1,323 K with strain rate of 10 s^{-1} and (*B*) 1,323 K with strain rate of 0.001 s^{-1}.

(*A*)

(*B*)

and 0.1 s^{-1} (in high-efficiency domain), respectively, which reveal the homogeneous microstructure without any cracks. The microstructure of a deformed specimen at strain rate of 0.001 s^{-1} shows the coarsening of eutectic lamellae (shown in inset). This is attributed to the high temperature and longer time period for deformation that is due to lower strain rate. Where the dendritic structure changed to irregular morphology, it is attributed to the eutectic coarsening and diffusion across the interfaces driving the morphologies toward equilibrium shapes. In case of deformed specimen at 0.1 s^{-1} strain rate condition, the eutectic started to coarsen but not completely and also the dendritic structure retained its morphology. **Figure 6C** and **6D** shows the microstructure at 1,323 K at a strain rate of 10 s^{-1} and 1,173 K at a strain rate of 0.001 s^{-1}, respectively. The microstructure of a deformed specimen reveals cracks that confirm the instability of the processing condition. The cracks were noted to be propagated through the brittle Laves phase, which is shown in **figure 6C** (inset).

The diffusion of elements plays a major role in coarsening of eutectic and globularization. The specimens at higher temperature (1,323 K) are expected to have higher diffusion and are thus selected for the elemental distribution study at different phases. **Figure 7** shows the EDS mapping of deformed specimens at 1,323 K at strain rates of 10 s^{-1} (**fig. 7A**) and 0.001 s^{-1} (**fig. 7B**). It is to be noted that the lower and higher strain rate are selected because of the lower and higher time periods experienced at higher temperatures. It is observed that the primary phase is enriched with iron, nickel, and chromium, and the Laves phase is enriched with niobium. Cobalt did not exhibit a preference between the two phases. The elemental segregation pattern is same for both the strain rate conditions. **Figure 8** shows the elemental contribution in primary the dendritic phase (**fig. 8A**) and Laves phase (**fig. 8B**) in suction cast specimen and 1,323 K with different strain rate conditions. The elemental distribution in as-cast condition clearly indicates that the iron and chromium are enriched in the primary dendritic phase and niobium is enriched in the Laves phase. In the deformed specimen, the Laves phase composition clearly shows the increase in niobium and is more prominent in lower strain rate condition because it is exposed at this processing condition for a longer period of time. The depletion of niobium in the FCC phase at lower strain rate is more compared with the higher strain rate at 1,323 K, which may be attributed to the diffusion of niobium across the interface at small length scale at lower strain rates. Cobalt percentage is similar in both suction cast and 1,323 K exposed with different strain rate conditions. In general, it is observed that the iron, nickel, and chromium are depleted and that niobium is enriched in the Laves phase at 1,323 K deformed condition. Hence, it is confirmed that the Laves phase is of the Co_2Nb type as reported in previous studies.[14]

FINITE ELEMENT SIMULATION AND CORRELATION WITH HARDNESS VARIATION

The finite element simulation was carried out to identify the strain field distribution within the specimen. The simulation was carried out using Simufact forming software with cylindrical geometry with quadrilateral mesh.

FIG. 8

Compositional variation in (A) FCC phase and (B) Laves phase, where 1,323@0.001 implies the temperature for hot deformation is 1,323 K and the strain rate is 0.001 s^{-1} and similarly for other labels.
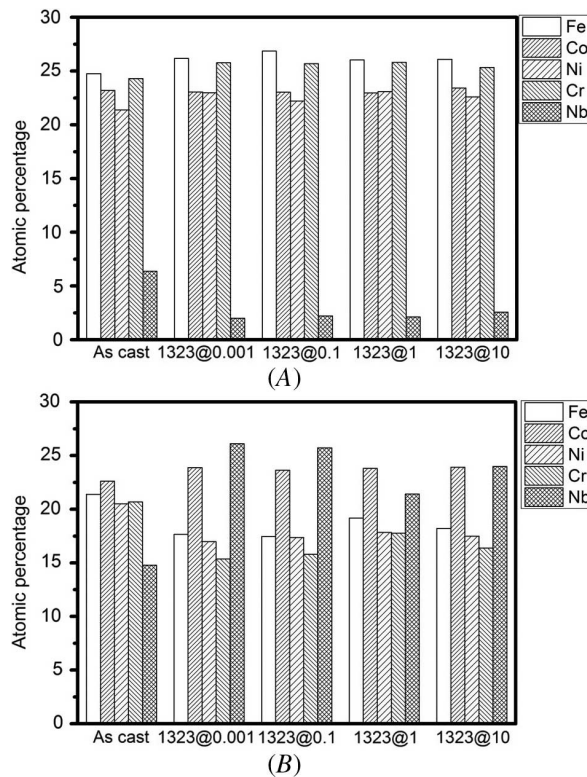

A mesh size of 0.025 mm was used with 42,840 elements. The friction between the anvil and the specimen was taken as intermediate value with an interface friction factor of 0.5. An isothermal condition was used and the material mechanical properties were taken from the experimentally obtained flow curves. The other physical properties are calculated by rule of mixture. **Figure 9** shows the strain field distribution at 1,323 K at stable and unstable conditions in the processing maps. **Figure 9A** and **9B** show the simulated strain field distribution

FIG. 9 Strain field distribution at 1,323 K with strain rates of (A) 0.1 s^{-1} and (B) 10 s^{-1} at a true strain of 0.69, where the height of the specimen after deformation is 4.5 mm.
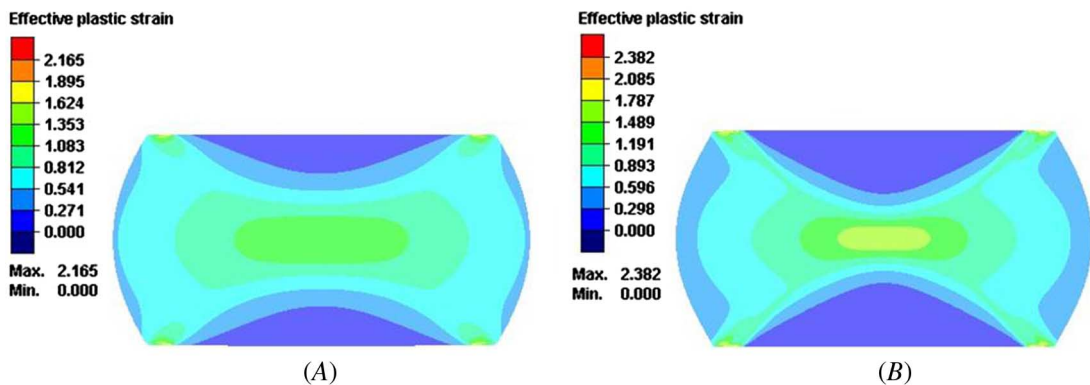
at 1,323 K with strain rates of 0.1 and 10 s^{-1}, respectively. It is clear from the simulated strain field distribution that the central region of the deformed specimen experienced higher strain, whereas the regions of the specimen closer to the contact with the anvil exhibit lower strain. The contact area is characterized by the near-dead metal zone, and its spread depends strongly on the strain rate used. The strain achieved in the central region of the specimen is more in the case of a strain rate condition of 10. The dead metal zone area is also large in the case of a strain rate condition of 10. It is obvious that increase of the strain further in 10 strain rate condition will experience shearing of specimen first as compared to 0.1 strain rate condition. The strain field distribution, which was predicted by integrating experimental data with the finite element simulation method, helps to optimize the geometrical design of the final product, which undergoes hot deformation. The microstructure of the specimen varies based on these strain field distributions, which are reflected in the microhardness of the specimen. The microhardness values are taken in the deformed specimen along the compression axis and perpendicular to the compression axis (marked as a brown line in fig. 10). The microhardness obtained here is the composite effect of primary phase and eutectic region as well as the coarsening of lamellar eutectic and strain field distribution inside the specimen. The microhardness distribution shows high hardness at the center that decreases toward the barreled area, which matches the high-strained center region and lower-strained barreled region. It is evident that the

FIG. 10 Microhardness variation along the width and height of the specimen (marked as brown lines) at 1,323 K with strain rates of 0.1 and 10 s^{-1}.
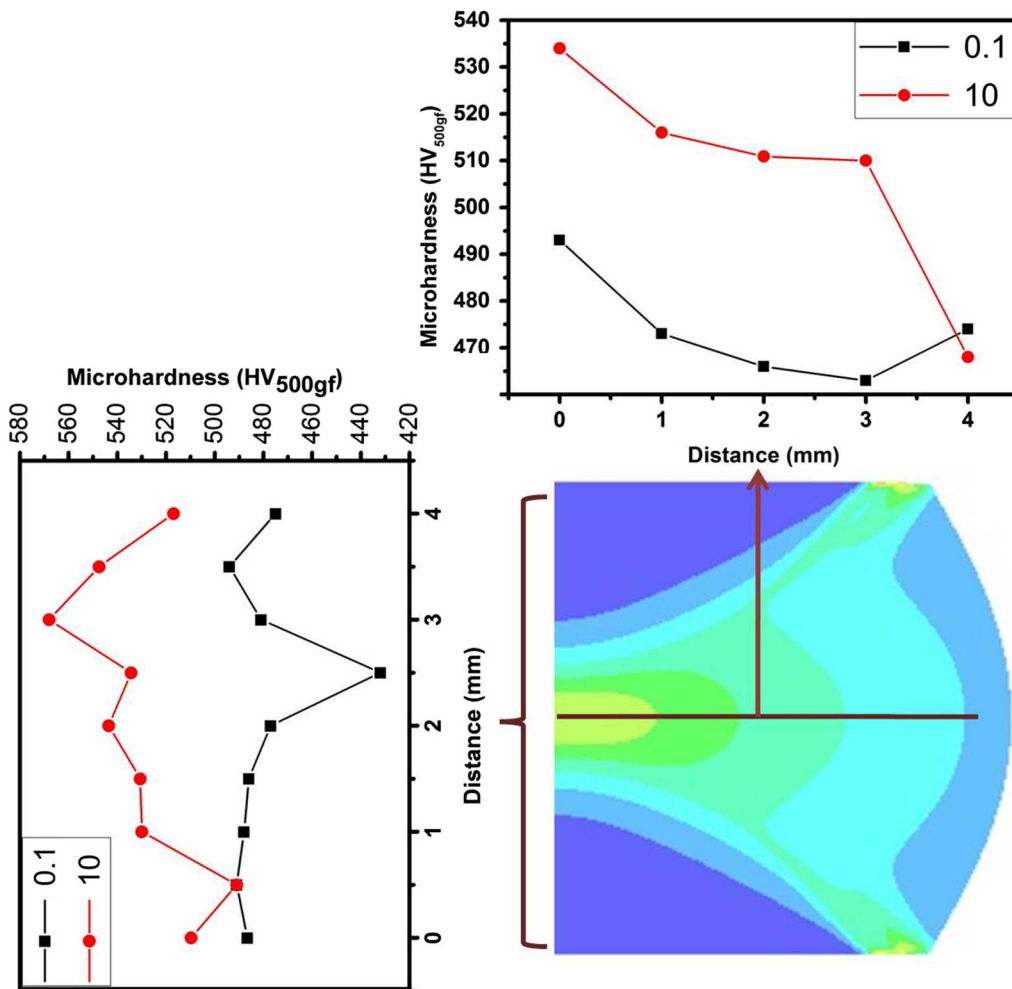
hardness at a high strain rate condition is greater than that at a lower strain rate condition, which may be attributed to the lower coarsening rate of eutectic as well as the deformation mechanism. It is found that the hardness at the maximum-strained center region at a strain rate of 10 s^{-1} ($\sim$530 HV) is more when compared with the strain rate of 0.1 s^{-1} ($\sim$490 HV). It is important to note that the integration of the deformation processing maps and FEM simulation leads to defect-free product development of HEAs that can be considered as potential candidates for high-temperature structural applications.

Conclusion

An EHEA with primary FCC and eutectic region (FCC + Laves) was made. The bulk hot forming processing of EHEA studies different strain rates and temperature conditions. The constitutive model developed for the currently studied EHEA at strain condition of 0.65 is shown in equation (8).

The optimum processing window based on the processing map for the presently studied EHEA is identified as being above 1,250 K with strain rate 0.1–1 s^{-1} as well as 1,175–1,200 K with strain rate 0.001–0.01 s^{-1}. The elemental distribution shows the enrichment of niobium in the Laves phase at a high temperature, and the lamellar morphology coarsens during the high-temperature deformation. The experimental studies and computer simulations have been integrated and validated. The integration of FEM simulation to identify the strain field distribution and the processing map distribution can contribute to the ICME platform for the development of products with complex geometry.

References

1. J.-W. Yeh, S.-K. Chen, S.-J. Lin, J.-Y. Gan, T.-S. Chin, T.-T. Shun, C.-H. Tsau, and S.-Y. Chang., "Nanostructured High-Entropy Alloys with Multiple Principal Elements: Novel Alloy Design Concepts and Outcomes," *Advanced Engineering Materials* 6, no. 5 (May 2004): 299–303. https://doi.org/10.1002/adem.200300567
2. D. B. Miracle and O. N. Senkov, "A Critical Review of High Entropy Alloys and Related Concepts," *Acta Materialia* 122 (January 2017): 448–511. https://doi.org/10.1016/j.actamat.2016.08.081
3. R. B. Nair, H. S. Arora, S. Mukherjee, S. Singh, H. Singh, and H. S. Grewal, "Exceptionally High Cavitation Erosion and Corrosion Resistance of a High Entropy Alloy," *Ultrasonics Sonochemistry* 41 (March 2018): 252–260. https://doi.org/10.1016/j.ultsonch.2017.09.044
4. L. Zhang, Y. Zhou, X. Jin, X. Du, and B. Li, "The Microstructure and High-Temperature Properties of Novel Nano Precipitation-Hardened Face Centered Cubic High-Entropy Superalloys," *Scripta Materialia* 146 (March 2018): 226–230. https://doi.org/10.1016/j.scriptamat.2017.12.001
5. Y. J. Kwon, J. W. Won, S. H. Park, J. H. Lee, K. R. Lim, Y. S. Na, and C. S. Lee, "Ultrahigh-Strength CoCrFeMnNi High-Entropy Alloy Wire Rod with Excellent Resistance to Hydrogen Embrittlement," *Materials Science and Engineering: A* 732 (August 2018): 105–111. https://doi.org/10.1016/j.msea.2018.06.086
6. L. Zhang, Y. Zhou, X. Jin, X. Du, and B. Li, "Precipitation-Hardened High Entropy Alloys with Excellent Tensile Properties," *Materials Science and Engineering: A* 732 (August 2018): 186–191. https://doi.org/10.1016/j.msea.2018.06.102
7. R. R. Boyer, "An Overview on the Use of Titanium in the Aerospace Industry," *Materials Science and Engineering: A* 213, nos. 1–2 (August 1996): 103–114. https://doi.org/10.1016/0921-5093(96)10233-1
8. S. Antonov, M. Detrois, and S. Tin, "Design of Novel Precipitate-Strengthened Al-Co-Cr-Fe-Nb-Ni High-Entropy Superalloys," *Metallurgical and Materials Transactions A* 49, no. 1 (January 2018): 305–320. https://doi.org/10.1007/s11661-017-4399-9
9. Y. Tan, J. Li, J. Wang, M. Kolbe, and H. Kou, "Microstructure Characterization of $CoCrFeNiMnPd_x$ Eutectic High-Entropy Alloys," *Journal of Alloys and Compounds* 731 (January 2018): 600–611. https://doi.org/10.1016/j.jallcom.2017.09.057
10. L. Jiang, Z. Q. Cao, J. C. Jie, J. J. Zhang, Y. P. Lu, T. M. Wang, and T. J. Li, "Effect of Mo and Ni Elements on Microstructure Evolution and Mechanical Properties of the $CoFeNi_xVMo_y$ High Entropy Alloys," *Journal of Alloys and Compounds* 649 (November 2015): 585–590. https://doi.org/10.1016/j.jallcom.2015.07.185
11. Y. Lu, Y. Dong, S. Guo, L. Jiang, H. Kang, T. Wang, B. Wen, et al., "A Promising New Class of High-Temperature Alloys: Eutectic High-Entropy Alloys," *Scientific Reports* 4 (August 2014): 6200. https://doi.org/10.1038/srep06200
12. I. S. Wani, T. Bhattacharjee, S. Sheikh, P. P. Bhattacharjee, S. Guo, and N. Tsuji, "Tailoring Nanostructures and Mechanical Properties of $AlCoCrFeNi_{2.1}$ Eutectic High Entropy Alloy Using Thermo-Mechanical Processing," *Materials Science and Engineering: A* 675 (October 2016): 99–109. https://doi.org/10.1016/j.msea.2016.08.048
13. M. R. Rahul, S. Samal, and G. Phanikumar, "Effect of Niobium Addition in $FeCoNiCuNb_x$ High-Entropy Alloys," *Journal of Materials Research* 34, no. 5 (March 2019): 700–708. https://doi.org/10.1557/jmr.2019.36

14. F. He, Z. Wang, P. Cheng, Q. Wang, J. Li, Y. Dang, J. Wang, and C. T. Liu, "Designing Eutectic High Entropy Alloys of CoCrFeNiNb$_x$," *Journal of Alloys and Compounds* 656 (January 2016): 284–289. https://doi.org/10.1016/j.jallcom.2015.09.153

15. Y. Dong, Y. Lu, J. Kong, J. Zhang, and T. Li, "Microstructure and Mechanical Properties of Multi-Component AlCrFeNiMo$_x$ High-Entropy Alloys," *Journal of Alloys and Compounds* 573 (October 2013): 96–101. https://doi.org/10.1016/j.jallcom.2013.03.253

16. W. Huo, H. Zhou, F. Fang, X. Zhou, Z. Xie, and J. Jiang, "Microstructure and Properties of Novel CoCrFeNiTa$_x$ Eutectic High-Entropy Alloys," *Journal of Alloys and Compounds* 735 (February 2018): 897–904. https://doi.org/10.1016/j.jallcom.2017.11.075

17. W. Huo, H. Zhou, F. Fang, Z. Xie, and J. Jiang, "Microstructure and Mechanical Properties of CoCrFeNiZr$_x$ Eutectic High-Entropy Alloys," *Materials & Design* 134 (November 2017): 226–233. https://doi.org/10.1016/j.matdes.2017.08.030

18. F. He, Z. Wang, X. Shang, C. Leng, J. Li, and J. Wang, "Stability of Lamellar Structures in CoCrFeNiNb$_x$ Eutectic High Entropy Alloys at Elevated Temperatures," *Materials & Design* 104 (August 2016): 259–264. https://doi.org/10.1016/j.matdes.2016.05.044

19. F. He, Z. Wang, S. Niu, Q. Wu, J. Li, J. Wang, C. T. Liu, and Y. Dang, "Strengthening the CoCrFeNiNb$_{0.25}$ High Entropy Alloy by FCC Precipitate," *Journal of Alloys and Compounds* 667 (January 2016): 53–57. https://doi.org/10.1016/j.jallcom.2016.01.153

20. Y. V. R. K. Prasad, K. P. Rao, and S. Sasidara, *Hot Working Guide: A Compendium of Processing Maps* (Materials Park, OH: ASM International, 2015).

21. S. L. Semiatin and J. J. Jonas, *Formability and Workability of Metals: Plastic Instability and Flow Localization* (Materials Park, OH: American Society for Metals, 1984).

22. S. Samal, M. R. Rahul, R. S. Kottada, and G. Phanikumar, "Hot Deformation Behaviour and Processing Map of Co-Cu-Fe-Ni-Ti Eutectic High Entropy Alloy," *Materials Science and Engineering: A* 664 (May 2016): 227–235. https://doi.org/10.1016/j.msea.2016.04.006

23. C. M. Sellars and W. J. McTegart, "On the Mechanism of Hot Deformation," *Acta Metallurgica* 14, no. 9 (September 1966): 1136–1138. https://doi.org/10.1016/0001-6160(66)90207-0

24. H. Mirzadeh, J. M. Cabrera, and A. Najafizadeh, "Constitutive Relationships for Hot Deformation of Austenite," *Acta Materialia* 59, no. 16 (September 2011): 6441–6448. https://doi.org/10.1016/j.actamat.2011.07.008

25. B. Nithin, K. Chattopadhyay, and G. Phanikumar, "Characterization of the Hot Deformation Behavior and Microstructure Evolution of a New γ-γ′ Strengthened Cobalt-Based Superalloy," *Metallurgical and Materials Transactions A* 49, no. 10 (October 2018): 4895–4905. https://doi.org/10.1007/s11661-018-4795-9

26. S. Venugopal, S. L. Mannan, and Y. V. R. K. Prasad, "Optimization of Cold and Warm Workability in Stainless Steel Type AISI 316L Using Instability Maps," *Journal of Nuclear Materials* 227, nos. 1–2 (December 1995): 1–10. https://doi.org/10.1016/0022-3115(95)00154-9

27. J. C. Malas and V. Seetharaman, "Using Material Behavior Models to Develop Process Control Strategies," *JOM* 44, no. 6 (June 1992): 8–13. https://doi.org/10.1007/BF03222246

28. S. Venugopal, S. L. Mannan, and Y. V. R. K. Prasad, "Criteria for Prediction of Flow Instabilities and Microstructural Manifestations during Warm Working of AISI 304L Stainless Steel," *Materials Science and Technology* 9, no. 11 (July 1993): 1021–1030. https://doi.org/10.1179/mst.1993.9.11.1021

29. M. R. Rahul, S. Samal, S. Venugopal, and G. Phanikumar, "Experimental and Finite Element Simulation Studies on Hot Deformation Behaviour of AlCoCrFeNi$_{2.1}$ Eutectic High Entropy Alloy," *Journal of Alloys and Compounds* 749 (June 2018): 1115–1127. https://doi.org/10.1016/j.jallcom.2018.03.262